RSC Advances

PAPER

View Article Online
View Journal | View Issue

Cite this: *RSC Adv.*, 2017, **7**, 5800

PdCu alloy nanodendrites with tunable composition as highly active electrocatalysts for methanol oxidation†

Yaling Xiong,‡[a] Wenying Ye,‡[a] Wenlong Chen,‡[b] Yiwen Wu,[a] Qingfeng Xu,[a] Yucong Yan,[a] Hui Zhang,*[a] Jianbo Wu*[b] and Deren Yang*[a]

Metal nanodendrites composed of highly branched arms have received great attention as electrocatalysts owing to their reasonably large surface area and the potential existence of low-coordinated sites in high densities. Although significant progress has been made in the synthesis of bimetallic nanodendrites, few works involve a system consisting of Pd and Cu, particularly in the case of alloyed nanodendrites. Here, we report a facile and powerful approach for the synthesis of PdCu alloy nanodendrites with tunable composition through varying the molar ratio of the Pd and Cu salt precursors. The key to achieving PdCu alloy nanodendrites is the use of $W(CO)_6$, which serves as a strong reducing agent. In addition, variation in the molar ratio of the precursors, from Pd rich to Cu rich, leads to shape evolution of the PdCu alloy, moving from a polyhedral to a dendritic nanostructure. This result indicates that galvanic replacement between a Cu rich alloy and a Pd precursor also plays an important role in the formation of PdCu alloy nanodendrites. When used as electrocatalysts for the methanol oxidation reaction (MOR), PdCu alloy nanodendrites exhibit remarkably enhanced catalytic properties relative to commercial Pd/C. Specifically, $Pd_{35}Cu_{65}$ alloy nanodendrites show the highest specific activity and mass activity for the MOR, 9.3 and 7.6 times higher than that of commercial Pd/C, respectively. This enhancement can be attributed to their dendritic structure and a possible bifunctional mechanism between Pd and Cu.

Received 27th October 2016
Accepted 26th December 2016

DOI: 10.1039/c6ra25900f

www.rsc.org/advances

Introduction

Proton exchange membrane fuel cells (PEMFCs) provide a direct way to convert the chemical energy of various fuels (*e.g.*, hydrogen, methanol, and formic acid) into electricity at low temperature without combustion that has several features, including high energy conversion efficiency, high power density, and low pollutant emission.[1,2] These advantages make PEMFCs an attractive candidate to be a clean and sustainable energy solution in both electric vehicles and portable electronics.[3,4] Among various types of fuel cells, direct methanol fuel cells (DMFCs), operated through the direct use of methanol as an electrochemically active fuel at the anode, are of particular interest since they can further circumvent the problems of hydrogen storage and transportation in PEMFCs.[5–7] Up to now, Pt-based nanoparticles have been proven to be the most effective monometallic catalyst for the methanol oxidation reaction (MOR) at the anode in DMFCs, because Pt sites are remarkably active for methanol adsorption and dissociation.[8,9] However, the rapidly increasing price and severely limited reserves of this metal are major obstacles to its commercial application in DMFCs.[10–12] In general, there are two main strategies to address the aforementioned issues. One is to enhance the catalytic performance and utility efficiency of Pt through size and shape control, as well as structure and composition design.[13–20] The other is the pursuance of a promising substitute for Pt as the catalyst in DMFCs without compromising on the relevant properties. Pd is believed to be a suitable replacement for Pt due to its excellent potential for improving catalytic properties towards the MOR in alkaline media, and it is at least 50 times more abundant than Pt.[21–23]

Recently, introducing a second metal (*e.g.*, Au, Ag, Ni or Cu) to form Pd-based bimetallic nanostructures has been considered as an effective strategy to improve catalytic performance, because of bifunctional mechanisms and/or ligand effects.[24–28] As a relatively less expensive and earth-abundant metal, Cu is a particularly promising candidate for generating PdCu bimetallic-based catalysts.[29,30] In addition to composition

[a]State Key Laboratory of Silicon Materials, School of Materials Science & Engineering, Cyrus Tang Center for Sensor Materials and Applications, Zhejiang University, Hangzhou, Zhejiang 310027, People's Republic of China. E-mail: msezhanghui@zju.edu.cn; mseyang@zju.edu.cn

[b]State Key Laboratory of Metal Matrix Composites, School of Materials Science and Engineering, Shanghai Jiao Tong University, 800 Dongchuan Rd, Shanghai, 200240, People's Republic of China. E-mail: jianbowu@sjtu.edu.cn

† Electronic supplementary information (ESI) available. See DOI: 10.1039/c6ra25900f

‡ These authors contributed equally to this work.

variation, tuning the shape and/or structure of PdCu-based catalysts is also of great importance in enhancing their catalytic properties toward the MOR, due to its well-known structural sensitivity.[31–34] As such, strong efforts have been employed towards developing the shape-controlled synthesis of PdCu bimetallic nanocrystals with improved performance.[35–38] Among various shapes, catalysts with a dendritic nanostructure are expected to be promising because of attractive structural features, such as porosity, high surface area, an interconnected nanostructure, and excellent electrical connectivity, which have received unprecedented interest in catalysis.[39–41] For example, Xia and co-workers demonstrated the synthesis of PdPt bimetallic nanodendrites with substantially enhanced catalytic properties towards the oxygen reduction reaction relative to commercial Pt/C *via* seeded growth.[42] In a recent study, we reported the synthesis of RhPd nanodendrites, through a co-reduction reaction, as highly active and durable electrocatalysts for the oxygen reduction reaction.[43] Both of these dendritic structures were formed through diffusion-limited aggregation owing to high supersaturation achieved in the initial stage of the reaction. Although significant progress has been made in the synthesis of bimetallic nanodendrites, producing PdCu bimetallic nanodendrites has met with limited success, probably due to the difficulty in achieving high supersaturation during the reaction, arising from the low redox potential of Cu^{2+}/Cu.

Here, we report a facile, one-step approach for the synthesis of PdCu alloy nanodendrites with controllable composition in benzyl alcohol, with $W(CO)_6$ as a strong reducing agent. PdCu alloy nanodendrites exhibit substantially enhanced catalytic properties towards the MOR in alkaline media relative to commercial Pd/C.

Experimental section

Chemicals and materials

Copper(II) acetylacetonate ($Cu(acac)_2$, 99%), palladium(II) acetylacetonate ($Pd(acac)_2$, 99%), polyvinyl pyrrolidone (PVP, MW $\approx$ 29 000), and tungsten hexacarbonyl ($W(CO)_6$, 97%) were purchased from Sigma-Aldrich. Commercial Pd/C (10 wt%) was purchased from Alfa Aesar. Benzyl alcohol (AR), ethanol (AR), and acetone (AR) were purchased from Sinopharm Chemical Reagent Co., Ltd. All chemicals were used without further purification.

Synthesis of PdCu alloy nanodendrites

In a standard procedure, 13 mg of $Cu(acac)_2$, 15 mg of $Pd(acac)_2$, and 50 mg of PVP were dissolved in 10 mL of benzyl alcohol under magnetic stirring at room temperature for 1 h. The resulting homogeneous solution was transferred into a 25 mL round-bottom flask. After that, 100 mg of $W(CO)_6$ was added into the flask under an Ar atmosphere. The reaction mixture was then sealed and heated at 140 °C for 2 h before it was cooled down to room temperature. Finally, the solution was centrifuged at 10 000 rpm and washed three times with ethanol before characterization.

Morphological, structural, and compositional characterization

The obtained samples were characterized using X-ray powder diffraction (XRD), using a Rigaku D/max-ga X-ray diffractometer with graphite monochromatized Cu Kα radiation (λ = 1.54178 Å). Transmission electron microscopy (TEM) images were taken using a HITACHI HT-7700 microscope operated at 100 kV. High-resolution transmission electron microscopy (HRTEM), high-angle annular dark-field scanning TEM (HAADF-STEM), and energy dispersive X-ray (EDX) mapping analyses were performed using an FEI Tecnai G2 F20 microscope operated at 200 kV. The percentages of Pd and Cu in the samples were determined using inductively coupled plasma atomic emission spectrometry (ICP-AES, IRIS Intrepid II XSP, TJA Co., USA). Thermogravimetric analysis (TGA) was performed with a thermogravimetric analyzer (SDT Q600). The temperature was monitored from room temperature to 800 °C, with a scan rate of 10 °C min^{-1}.

Preparation of carbon-supported catalysts

In a standard preparation, carbon black (Vulcan XC72) was dispersed in ethanol and sonicated for 30 min. A designated amount of PdCu particles was added to this dispersion, with a PdCu/C mass ratio of 20 : 80. This mixture was further sonicated for 10 min and stirred for 24 h. After that, the resultant solids were precipitated out using centrifugation and washed three times with ethanol.

Electrochemical measurements

A three-electrode cell with an electrochemical workstation (CHI 760E) was used to measure the electrochemical performance of the PdCu/C catalysts, including the commercial Pd/C. A glassy-carbon rotating disk electrode (RDE, Pine Research Instrumentation, United States) was used as the working electrode (area: ~0.196 cm^2). An Ag/AgCl electrode and a Pt mesh (1 × 1 cm^2) connected to a Pt wire were used as the reference and counter electrodes, respectively. To make a catalyst ink, 5 mg of PdCu/C catalyst was dispersed in 10 mL of mixed solvent and sonicated for 10 min. The solvent contained a mixture of de-ionized water, isopropanol, and 5% Nafion 117 solution at the volumetric ratio of 8 : 2 : 0.05. After that, 60 μL of the catalyst ink was added onto the RDE and dried under air flow for 30 min to make the working electrode. The electrochemical active surface area (ECSA) was determined from the cyclic voltammogram (CV) curves, calculating the amount of charge through integrating the hydrogen desorption region after double layer correction. The CV measurements were carried out in Ar-saturated 0.1 M KOH solution at room temperature with a scan rate of 50 mV s^{-1}, and before the test Ar purging was conducted for 30 min. For the electrooxidation of methanol, CV curves were recorded in an Ar-purged 0.1 M KOH/0.5 M CH_3OH solution at a sweep rate of 50 mV s^{-1} in the range of 0.05 V to 1.2 V (*vs.* RHE).

Results and discussion

PdCu alloy nanodendrites were synthesized *via* the co-reduction of Pd and Cu salt precursors with $W(CO)_6$ in benzyl alcohol at

140 °C. Fig. 1 shows TEM, HRTEM, HAADF-STEM and EDX mapping images of the PdCu alloy nanodendrites, prepared using the aforementioned approach with a Pd/Cu molar ratio of 1 : 1 in the synthesis (*i.e.*, the standard procedure). As demonstrated in the TEM images in Fig. 1A and B, most of the nanocrystals were observed to have a dendritic structure with a flower-like shape. Careful observation shows that the dendrite is composed of numerous small particles of less than 10 nm in size. The overall size of the nanodendrite is ~30 nm. Fig. 1C shows a typical HRTEM image of an individual nanodendrite. It is clear that the nanodendrite is a polycrystal, consisting of single-crystalline particles (marked with circles). The fringes with a lattice spacing of 2.17 Å can be indexed to the {111} planes of face-centered cubic (fcc) Pd and/or Cu. The elemental distribution of the nanodendrite is determined using EDX mapping analysis (Fig. 1D). It is indicated that both Pd and Cu are distributed evenly throughout each PdCu nanodendrite, confirming an alloy structure. Moreover, the compositions of the PdCu nanodendrites were quantitatively measured using inductively coupled plasma atomic emission spectrometry (ICP-AES, Table S1†). The Pd/Cu atomic ratio of these nanodendrites was about 0.91 : 1 (*i.e.*, $Pd_{48}Cu_{52}$), which is consistent with the molar ratio of Pd and Cu salt precursors used in the synthesis.

The compositions of the PdCu alloy nanostructures were readily tuned by varying the amounts of Pd and Cu salt precursors supplied in the synthesis. On the basis of ICP-AES analysis, $Pd_{77}Cu_{23}$, $Pd_{65}Cu_{35}$, $Pd_{43}Cu_{57}$, and $Pd_{35}Cu_{65}$ alloy nanostructures were obtained when the molar ratio of the Pd and Cu precursors was varied from 4 : 1 to 2 : 1, 2 : 3, and 1 : 3 (Table S1†). Fig. 2 shows XRD patterns of these PdCu samples with different compositions, together with a Pd/C sample. From the XRD patterns, all the PdCu samples clearly show three well-defined diffraction peaks, corresponding to the (111), (200), and (220) planes of a single fcc lattice, suggesting the formation of an alloy structure. The diffraction peaks gradually shift to higher values of 2θ upon increasing the amount of Cu component, due to a decreased lattice constant arising from the smaller diameter of Cu atoms relative to Pd atoms. However, careful observation indicates that the {111} peaks are asymmetric and small diffraction peaks associated with Cu_2O (marked by •) or pure Pd (marked by *) can be resolved. Exposure to oxygen and slight phase separation could be responsible for the impurities of Cu_2O and pure Pd. In addition, we found that the molar ratio of Pd and Cu salt precursors has a great influence on the morphology of the PdCu alloy nanostructures. Fig. 3 shows typical TEM images of PdCu alloy nanostructures with different compositions. It is clear that the shape of the PdCu alloy nanostructures evolves from polyhedral to nanodendrite upon increasing the Cu content (Fig. 3A–D). The Cu-rich samples also prefer to adopt a dendritic shape with longer branched arms.

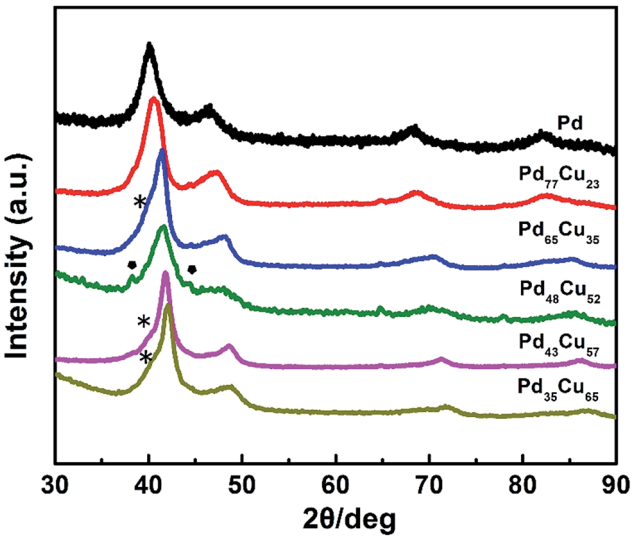

Fig. 2 XRD patterns of PdCu alloy nanostructures with different compositions, including commercial Pd/C.

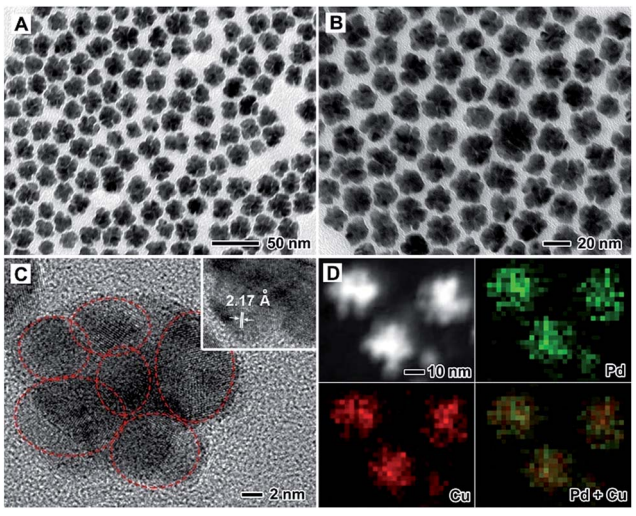

Fig. 1 (A, B) TEM, (C) HRTEM, and (D) HAADF-STEM-EDX mapping images of PdCu alloy nanodendrites prepared using the standard procedure, with a Pd/Cu molar ratio of 1 : 1 used in the synthesis. The inset of (C) corresponds to the HRTEM image at a higher magnification. The green and red correspond to Pd and Cu elements, respectively.

In order to decipher the growth mechanism of the PdCu nanodendrites, a series of samples obtained at different stages during the synthesis of $Pd_{48}Cu_{52}$ nanodendrites (*i.e.*, the standard procedure) were collected for TEM and ICP-AES analyses. In the initial stage of the reaction ($t = 2.5$ min), a Pd-rich sample with a composition of $Pd_{83}Cu_{17}$ (see Fig. S1†) was generated due to the easier reduction of the Pd precursor relative to the Cu precursor, arising from the larger redox potential of Pd^{2+}/Pd (0.951 V *versus* RHE) compared to Cu^{2+}/Cu (0.342 V *versus* RHE). However, the morphology of the product at this time cannot be revealed using TEM due to the difficulty in precipitating the sample *via* centrifugation, as a result of the very small particle size. As the reaction continued to $t = 5$ min, numerous small PdCu particles were generated (Fig. 4A). From ICP-AES analysis shown in Fig. S1,† these particles are composed of $Pd_{55}Cu_{45}$ with a remarkable increase in the Cu content. As is well-known, $Cu(acac)_2$ is very difficult to directly reduce to Cu due to the small redox potential of Cu^{2+}/Cu, resulting in the low Cu

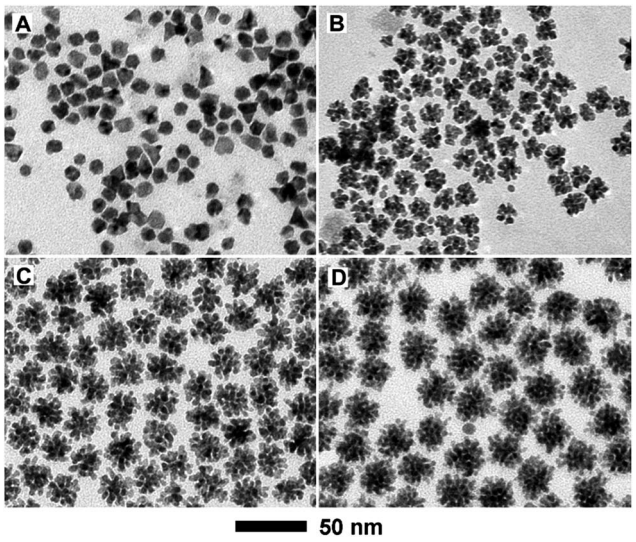

Fig. 3 TEM images of PdCu alloy nanostructures with different compositions prepared using the standard procedure, except with a different molar ratio of Pd and Cu salt precursors supplied in the synthesis: (A) 4 : 1; (B) 2 : 1; (C) 2 : 3; and (D) 1 : 3.

content of the final product. For a system involving Pd and Cu, however, underpotential deposition (UPD) and galvanic replacement usually happen during nanocrystal growth, which was also observed in the synthesis of PdCu tripods.[36] As a result, the initially formed Pd-rich particles induce the reduction of Cu^{2+} ions by taking advantage of Cu UPD, resulting in an increase in Cu content in the PdCu alloy. When the reaction proceeded to $t = 10$ min, dendritic structures with a composition of $Pd_{54}Cu_{46}$ were formed (Fig. 4B). Similar to our previous results for the synthesis of PtCu nanodendrites,[44] the generation of PdCu nanodendrites can be attributed to galvanic replacement between the initially formed PdCu alloy with high Cu content and Pd^{2+} ions in solution, which generally results in dendritic structures.[45] This demonstration is also supported by the morphology variation between different Pd/Cu compositions, in which the Cu-rich samples facilitate galvanic replacement and thus prefer to adopt a dendritic shape. With an extension of the reaction time (*e.g.*, 30 and 60 min), the branches of the nanodendrites grew up, resulting in the formation of nanodendrites of high-quality (Fig. 4C and D). The composition of the PdCu nanodendrites is an atomic ratio of about 1 (Fig. S1†), close to the feeding ratio of the Pd and Cu salt precursors. Taken together, Cu UPD and galvanic replacement play an important role in the formation of PdCu nanodendrites with a Pd/Cu atomic ratio close to 1.

In addition to Cu UPD and galvanic replacement, the type of reducing agent used, with different reducing power, is also of great importance to the formation of PdCu nanodendrites. In the absence of $W(CO)_6$ (Fig. 5A), nanoparticles with a polyhedral shape instead of a dendritic structures are generated, with benzyl alcohol as a mild reducing agent. When replacing $W(CO)_6$ with citric acid (Fig. 5B), the products are also dominated by polyhedra. In this case, benzyl alcohol still acts as a reducing agent in the presence of citric acid, due to the stronger reducing power of benzyl alcohol compared to citric acid. When introducing ascorbic acid as a reducing agent (Fig. 5C), two kinds of irregular particles co-exist in the final product. Similarly, when using $Co_2(CO)_8$ instead of $W(CO)_6$ (Fig. 5D), a large number of small particles are obtained, since the overly strong reducing activity of cobalt carbonyl results in rapid and substantial nucleation. These results indicate that the use of $W(CO)_6$ as a reducing agent is indispensable for the formation of PdCu nanodendrites. It is well-known that $W(CO)_6$ is easily decomposed into W and CO at a relatively elevated temperature and then the *in situ* generated W acts as a reducing agent for the shape-controlled synthesis of noble-metal

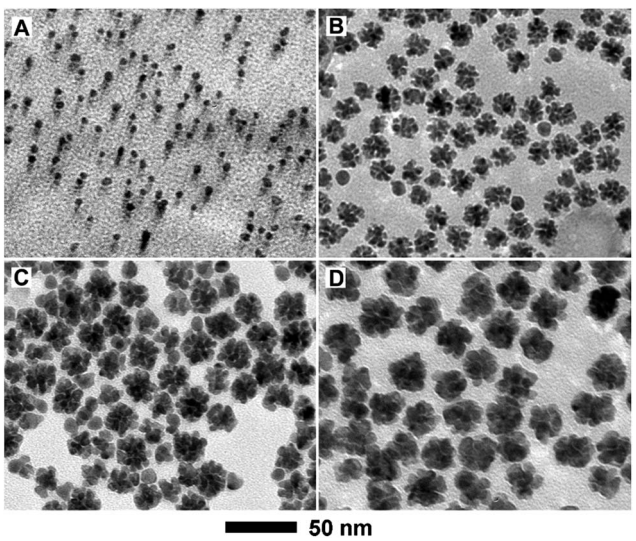

Fig. 4 TEM images of PdCu nanostructures prepared using the standard procedure, except with different periods of reaction time: (A) 5; (B) 10; (C) 30; and (D) 60 min.

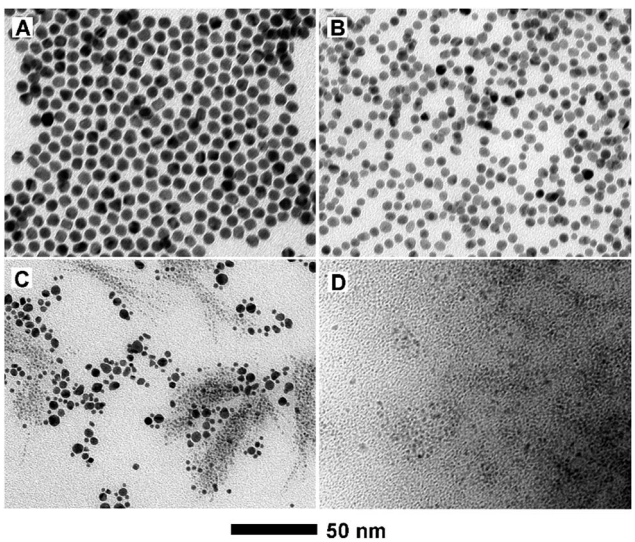

Fig. 5 TEM images of products prepared using the standard procedure, except for the use of different reducing agents: (A) in the absence of $W(CO)_6$, (B) replacing $W(CO)_6$ with citric acid, (C) replacing $W(CO)_6$ with ascorbic acid, and (D) replacing $W(CO)_6$ with $Co_2(CO)_8$.

nanocrystals.[46] The essence of the issue is the reasonable control of the reduction rate of Pd^{2+} and Cu^{2+} ions.

The as-prepared PdCu alloy nanocrystals with different components were separately loaded on carbon black support (Vulcan XC-72) and then evaluated as electrocatalysts for the MOR with commercial Pd/C serving as the benchmark. Fig. S2† shows cyclic voltammograms (CV) from these six catalysts recorded in Ar-purged 0.1 M KOH aqueous solution. The potential region from 0.1 to 0.4 V was attributed to the H-desorption/absorption process. However, there were no obvious H-desorption peaks for most catalysts that were similar to other literature reports previously.[31,34,35] The peaks at around 0.65 V and 0.92 V correspond to the oxidation of Cu and Pd, respectively. It is generally known that the electrochemically active surface areas (ECSAs) are calculated by integrating the electric charge associated with the hydrogen absorption area.[47] As summarized in Table S1,† the ECSAs (normalized to Pd) of $Pd_{77}Cu_{23}$, $Pd_{65}Cu_{35}$, $Pd_{48}Cu_{52}$, $Pd_{43}Cu_{57}$ and $Pd_{35}Cu_{65}$ supported on carbon are about 23.12, 34.16, 40.49, 23.89 and 24.82 $m^2\ g^{-1}$, respectively, most of which are a little lower than for commercial Pd/C (33.0 $m^2\ g^{-1}$), probably due somewhat to aggregation during the preparation of the catalysts, and organic species (*e.g.*, PVP and benzyl alcohol) deposited on their surfaces during synthesis.[34,48] These PdCu catalysts were washed several times and treated with *tert*-butylamine and $NaBH_4$ to remove residual capping agent, however a few bands associated with these species are still visible (see the Fourier transform infrared spectroscopy spectra in Fig. S3†).

The electrocatalytic properties of the PdCu alloy nanodendrites toward the MOR were measured in 150 mL of solution containing 0.1 M KOH and 0.5 M CH_3OH at a sweep rate of 50 mV s^{-1} and were compared with those of commercial Pd/C catalysts (Fig. 6). As observed in Fig. 6A and C, all of the PdCu alloy catalysts show improved specific activity and mass activity relative to commercial Pd/C, indicating that the incorporation of Cu into Pd can enhance the MOR properties. Among these, the $Pd_{35}Cu_{65}$ alloy nanodendrites exhibit the highest specific activity (0.540 mA cm^{-2}) and mass activity (0.135 mA μg_{Pd}^{-1}) at the forward-peak potential (Fig. 6C and D), 9.3 and 7.6 times higher than that of commercial Pd/C, respectively. For a better understanding of the activity of our own catalysts, a comparison with other typical PdCu and Pd/C catalysts is summarized in Table S2.† We find that the enhancement factor (with commercial Pd/C as a reference) of our $Pd_{35}Cu_{65}$ alloy nanodendrites ranked at the forefront, owing to the unique dendritic structure relative to other typical examples in the literatures.[49–54]

The long-term performance of PdCu alloy nanodendrites and Pd/C towards the MOR was evaluated in 0.1 M KOH and 0.5 M CH_3OH for 3000 s (Fig. 7). The current (normalized using Pd mass) obtained with the PdCu catalysts and commercial Pd/C decreased drastically due to adsorption of intermediates (*e.g.*, CO) on the surfaces, as reported in the literature.[55] After 1000 s, the currents decayed at a very slow rate and approached the limiting current at 3000 s (Fig. 7B). The limiting currents of the PdCu alloy nanodendrites are higher than for commercial Pd/C. The $Pd_{35}Cu_{65}$ catalyst exhibited the highest current in the entire

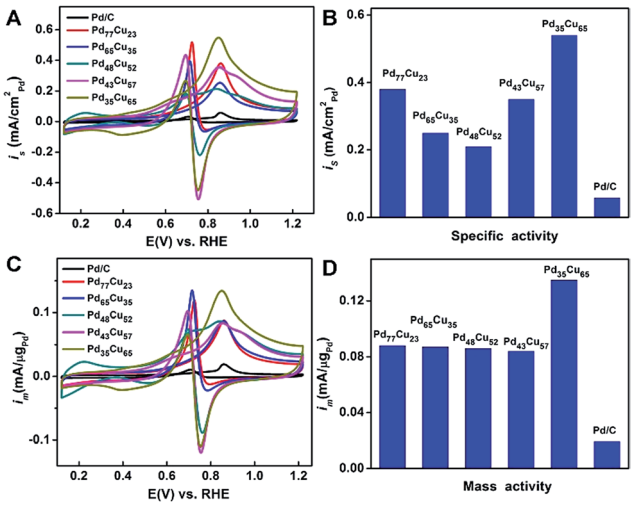

Fig. 6 (A) Cyclic voltammograms normalized using surface area, (B) specific activity at the forward-peak potential, (C) cyclic voltammograms normalized using Pd mass, and (D) mass activity at the forward-peak potential of the five PdCu/C catalysts with different compositions including commercial Pd/C. The electro-oxidation of methanol was performed in Ar-saturated aqueous solution containing 0.1 M KOH/0.5 M CH_3OH at a sweep rate of 50 mV s^{-1}.

test time, implying that superior stability originates from a high Cu content, which could accelerate the oxidation of CO_{ads}.[50,56]

The enhanced performances of the PdCu alloy catalysts in the MOR can be attributed to a combination of a bifunctional mechanism and the unique dendritic structures.[39,57] In methanol electro-oxidation, reaction intermediates mainly containing CO_{ads} are inevitably generated, which severely poison the active sites by strongly adsorbing on the surface of the Pd sites.[55] The Cu component in the alloy can accelerate the oxidation of reaction intermediates, especially CO_{ads}, since Cu is more active than Pd for CO oxidation.[56] As such, this bifunctional effect can remove CO_{ads} intermediates on the Pd sites, which substantially enhances the catalytic properties of PdCu alloy catalysts towards the MOR. In addition, the unique dendritic structures, generally containing some high-index facets and defects, also play an important role in enhancing the catalytic properties towards the MOR.[43]

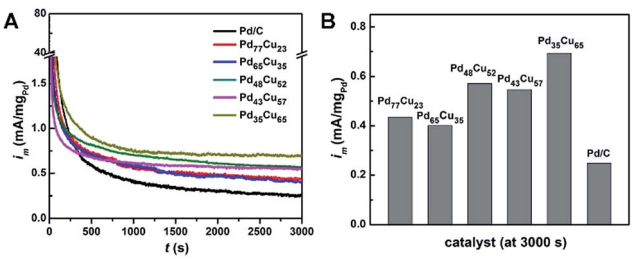

Fig. 7 (A) Chronoamperometric measurements of PdCu/C catalysts with different compositions including commercial Pd/C in Ar-saturated aqueous solution containing 0.1 M KOH/0.5 M CH_3OH at a sweep rate of 50 mV s^{-1}. (B) Current normalized using Pd mass at 3000 s.

Conclusions

In summary, PdCu alloy nanodendrites with tunable composition have been synthesized through the co-reduction of Pd and Cu salt precursors at different molar ratios using $W(CO)_6$ as a strong reducing agent. We found that high supersaturation during the reaction, arising from the strong reducing agent, and galvanic replacement between the Cu rich alloy and Pd precursor might play key roles in facilitating the formation of such nanodendrites. In addition, electrochemical measurements indicate that the $Pd_{35}Cu_{65}$ alloy nanodendrites exhibit substantially enhanced catalytic properties in terms of specific and mass activities, relative to such nanodendrites with other compositions as well as commercial Pd/C, due to their unique structures and possible synergistic effects between these two metals. This work not only reports a facile approach for the synthesis of bimetallic alloy nanodendrites, but also provides an effective strategy to synthesize non-Pt MOR catalysts with enhanced catalytic performance.

Acknowledgements

The work on electron microscopy was carried out in the Center for Electron Microscopy of Zhejiang University. We acknowledge financial support by the National Science Foundation of China (51372222 and 51522103), the National Program for Support of Top-notch Young Professionals, the Fundamental Research Funds for the Central Universities (2015XZZX004-23), the Program for Innovative Research Teams in University of the Ministry of Education of China (IRT13R54), the thousand talents program for distinguished young scholars (JBW) from the National Science Foundation of China, and a start-up fund (JBW) from Shanghai Jiao Tong University.

Notes and references

1 B. Steele and A. Heinzel, *Nature*, 2001, **414**, 345–352.
2 M. Debe, *Nature*, 2012, **486**, 43–51.
3 M. Winter and R. Brodd, *Chem. Rev.*, 2004, **104**, 4245–4270.
4 M. Scofield, H. Liu and S. Wong, *Chem. Soc. Rev.*, 2015, **44**, 5836–5860.
5 S. Kamarudin, W. Daud, S. Ho and U. Hasran, *J. Power Sources*, 2007, **163**, 743–754.
6 C. Bianchini and P. Shen, *Chem. Rev.*, 2009, **109**, 4183–4206.
7 X. Zhao, M. Yin, L. Ma, L. Liang, C. Liu, J. Liao, T. Lu and W. Xing, *Energy Environ. Sci.*, 2011, **4**, 2736–2753.
8 J. Kua and W. Goddard III, *J. Am. Chem. Soc.*, 1999, **121**, 10928–10941.
9 N. Kakati, J. Maiti, S. Lee, S. Jee, B. Viswanathan and Y. Yoon, *Chem. Rev.*, 2014, **114**, 12397–12429.
10 H. Zhang, M. Jin and Y. Xia, *Chem. Soc. Rev.*, 2012, **41**, 8035–8049.
11 Y. Jia, Y. Jiang, J. Zhang, L. Zhang, Q. Chen, Z. Xie and L. Zheng, *J. Am. Chem. Soc.*, 2014, **136**, 3748–3751.
12 T. Takeguchi, T. Yamanaka, K. Asakura, E. Muhamad, K. Uosaki and W. Ueda, *J. Am. Chem. Soc.*, 2012, **134**, 14508–14512.
13 S. Maksimuk, S. Yang, Z. Peng and H. Yang, *J. Am. Chem. Soc.*, 2007, **129**, 8684–8685.
14 J. Wu, J. Zhang, Z. Peng, S. Yang, F. Wagner and H. Yang, *J. Am. Chem. Soc.*, 2010, **132**, 4984–4985.
15 S. Guo, S. Zhang, X. Sun and S. Sun, *J. Am. Chem. Soc.*, 2011, **133**, 15354–15357.
16 J. Wu, L. Qi, H. You, A. Gross, J. Li and H. Yang, *J. Am. Chem. Soc.*, 2012, **134**, 11880–11883.
17 B. Xia, H. Wu, X. Wang and X. Lou, *J. Am. Chem. Soc.*, 2012, **134**, 13934–13937.
18 J. Rossmeisl, P. Ferrin, G. Tritsaris, A. Nilekar, S. Koh, S. Bae, S. Brankovic, P. Strasser and M. Mavrikakis, *Energy Environ. Sci.*, 2012, **5**, 8335–8342.
19 Y. Qi, T. Bian, S. Choi, Y. Jiang, C. Jin, M. Fu, H. Zhang and D. Yang, *Chem. Commun.*, 2014, **50**, 560–562.
20 T. Bian, H. Zhang, Y. Jiang, C. Jin, J. Wu, H. Yang and D. Yang, *Nano Lett.*, 2015, **15**, 7808–7815.
21 E. Antolini, *Energy Environ. Sci.*, 2009, **2**, 915–931.
22 F. Liao, T. Lo and S. Tsang, *ChemCatChem*, 2015, **7**, 1998–2014.
23 A. Chen and C. Osrtom, *Chem. Rev.*, 2015, **115**, 11990–12044.
24 L. Fei, S. Zhong and A. Xu, *Angew. Chem., Int. Ed.*, 2013, **52**, 645–649.
25 S. Fu, C. Zhu, D. Du and Y. Lin, *ACS Appl. Mater. Interfaces*, 2015, **7**, 13842–13848.
26 M. Wang, W. Zhang, J. Wang, D. Wexler, S. Poynton, R. Slade, H. Liu, B. Jensen, R. Kerr, D. Shi and J. Chen, *ACS Appl. Mater. Interfaces*, 2013, **5**, 12708–12715.
27 V. Mazumder, M. Chi, M. Mankin, Y. Liu, O. Metin, D. Sun, K. More and S. Sun, *Nano Lett.*, 2012, **12**, 1102–1106.
28 Y. Zheng, S. Zhao, S. Liu, H. Yin, Y. Chen, J. Bao, M. Han and Z. Dai, *ACS Appl. Mater. Interfaces*, 2015, **7**, 5347–5357.
29 L. Yang, C. Hu, J. Wang, Z. Yang, Y. Guo, Z. Bai and K. Wang, *Chem. Commun.*, 2011, **47**, 8581–8583.
30 L. Zhang, F. Hou and Y. Tan, *Chem. Commun.*, 2012, **48**, 7152–7154.
31 Z. Yin, W. Zhou, Y. Gao, D. Ma, C. Kiely and X. Bao, *Chem.–Eur. J.*, 2012, **18**, 4887–4893.
32 C. Hu, Y. Guo, J. Wang, L. Yang, Z. Yang, Z. Bai, J. Zeng, K. Wang and K. Jiang, *ACS Appl. Mater. Interfaces*, 2012, **4**, 4461–4464.
33 Z. Shih, C. Wang, G. Xu and H. Chang, *J. Mater. Chem. A*, 2013, **1**, 4773–4778.
34 P. Xi, Y. Cao, F. Yang, C. Ma, F. Chen, S. Yu, S. Wang, Z. Zeng and X. Zhang, *Nanoscale*, 2013, **5**, 6124–6130.
35 Q. Gao, Y. Ju, D. An, M. Gao, C. Cui, J. Liu, H. Cong and S. Yu, *ChemSusChem*, 2013, **6**, 1878–1882.
36 L. Zhang, S. Choi, J. Tao, H. Peng, S. Xie, Y. Zhu, Z. Xie and Y. Xia, *Adv. Funct. Mater.*, 2014, **24**, 7520–7529.
37 Z. Zhang, J. Huang, L. Zhang, M. Sun, Y. Wang, Y. Lin and J. Zeng, *Nanotechnology*, 2014, **25**, 435602.
38 L. Zhang, H. Su, M. Sun, Y. Wang, W. Wu, T. Yu and J. Zeng, *Nano Res.*, 2015, **8**, 2415–2430.
39 B. Lim and Y. Xia, *Angew. Chem., Int. Ed.*, 2011, **50**, 76–85.
40 L. Wang, Y. Nemoto and Y. Yamauchi, *J. Am. Chem. Soc.*, 2011, **133**, 9674–9677.

41 A. Mohanty, N. Garg and R. Jin, *Angew. Chem., Int. Ed.*, 2010, **49**, 4962–4966.
42 B. Lim, M. Jiang, P. Camargo, E. Cho, J. Tao, X. Lu, Y. Zhu and Y. Xia, *Science*, 2009, **324**, 1302–1305.
43 Y. Qi, J. Wu, H. Zhang, Y. Jiang, C. Jin, M. Fu, H. Yang and D. Yang, *Nanoscale*, 2014, **6**, 7012–7018.
44 Y. Jiang, T. Bian, F. Lin, H. Zhang, C. Jin, Z. Li, D. Yang and Z. Zhang, *J. Mater. Chem. A*, 2015, **3**, 21284–21289.
45 L. Xiong, Y. Huang, X. Liu, G. Sheng, W. Li and H. Yu, *Electrochim. Acta*, 2013, **89**, 24–28.
46 J. Zhang and J. Fang, *J. Am. Chem. Soc.*, 2009, **131**, 18543–18547.
47 L. Yang, D. Yan, C. Liu, H. Song, Y. Tang, S. Luo and M. Liu, *J. Power Sources*, 2015, **278**, 725–732.
48 Z. Lin, W. Chen, Y. Jiang, T. Bian, H. Zhang, J. Wu, Y. Wang and D. Yang, *Nanoscale*, 2016, **8**, 12812–12818.
49 H. Mao, T. Huang and A. Yu, *Electrochim. Acta*, 2015, **174**, 1–7.
50 S. Arulmani, S. Krishnamoorthy, J. J. Wu and S. Anandan, *Electroanalysis*, 2016, **28**, 1–9.
51 M. Hsieh and T. Whang, *Appl. Surf. Sci.*, 2013, **270**, 252–259.
52 Z. Yin, H. Zheng, D. Ma and X. Bao, *J. Phys. Chem. C*, 2009, **113**, 1001–1005.
53 Z. Li, H. Gong, T. Mu and Y. Luan, *CrystEngComm*, 2014, **16**, 4038–4044.
54 X. Zhou, Y. Gan, Z. Dai and R. Zhang, *J. Electroanal. Chem.*, 2012, **685**, 97–102.
55 C. Bianchini and P. Shen, *Chem. Rev.*, 2009, **109**, 4183–4206.
56 K. Choi and M. Vannice, *J. Catal.*, 1991, **131**, 22–35.
57 H. Gasteiger, N. Markovic, P. Ross and E. Cairns, *J. Phys. Chem.*, 1993, **97**, 12020–12029.